JM RAPIDS

Scaling of flat plate drag reduction using plasma-generated streamwise vortices

Xiaohui Wei[1] and Yu Zhou[2,1]

[1]Center for Turbulence Control, Harbin Institute of Technology (Shenzhen), Shenzhen 518055, PR China

[2]School of Mechanical Engineering & Mechanics, College of Engineering, Eastern Institute of Technology, Ningbo 315000, PR China

Corresponding authors: Yu Zhou, yuzhou@eitech.edu.cn; Xiaohui Wei, weixiaohui17@mails.ucas.edu.cn

Skin-friction drag reduction (DR) in a turbulent boundary layer (TBL) using plasma-generated streamwise vortices (PGSVs) is governed by plasma-induced spanwise wall-jet velocity W, the distance L between the positive electrodes of two adjacent plasma actuators (PAs) and the friction Reynolds number Re_τ. It is found experimentally that DR increases logarithmically with the growing maximum spanwise mean velocity $\overline{W}_{max}^+$ but decreases with rising L^+ and Re_τ, where superscript '+' denotes normalization by the inner scales. It is further found from theoretical and empirical scaling analyses that the dimensionless drag variation $\Delta F = g_1(\overline{W}_{max}^+, L^+, Re_\tau)$ may be reduced to $\Delta F = g_2(\xi)$, where g_1 and g_2 are different functions and the scaling factor $\xi = [k_2 \log_{10}(k_1 \overline{W}_{max}^+)]/(L^+ Re_\tau)$ (k_2 and k_1 are constants) is physically the circulation of the PGSVs. Discussion is conducted based on $\Delta F = g_2(\xi)$, which provides important insight into the physics of TBL control based on PAs.

Key words: turbulent boundary layers, drag reduction, plasmas

1. Introduction

Skin-friction drag reduction (DR) in turbulent boundary layers (TBLs) has been pursued extensively since the late 1970s (Kline *et al.* 1967) and can be achieved passively or actively. Passive techniques involve surface modifications or coatings that alter the flow characteristics of the boundary layer, such as riblets (Choi *et al.* 1993), superhydrophobic surfaces (Rastegari & Akhavan 2015) and compliant surfaces (Fukagata *et al.* 2008). Active techniques, on the other hand, involve energy input, such as streamwise travelling waves (Quadrio *et al.* 2009), blowing (Cheng *et al.* 2021*a*) and dielectric barrier discharge plasma actuators (PAs) (Thomas *et al.* 2019; Cheng *et al.* 2021*b*). Among the active methods, the

PA has become one of the most popular techniques due to its simple structure, non-destructive to the structure that generates TBL and high DR. Cheng *et al.* (2021*b*) and Thomas *et al.* (2019) have perhaps carried out the two latest representative experimental investigations. The former studied three configurations of PA arrays that generated counter- or co-rotating large-scale streamwise vortices, achieving a maximum spatially averaged DR of 26 % downstream of the actuators at the friction Reynolds number $Re_\tau = 572$. It was later confirmed that the DR over the actuation region exceeded 70 % (Wei & Zhou 2024). Thomas *et al.* (2019) investigated two configurations of PA arrays that could generate counter- and co-rotating large-scale streamwise vortices, respectively, and obtained a spatially averaged DR over the actuation region in excess of 70 % at the momentum Reynolds number $Re_\theta = 4538$–18 500. They performed a quantitative analysis of the DR as a function of each individual parameter, i.e. the plasma-induced maximum spanwise mean velocity $\overline{W}_{max}^+$ and the distance L^+ between the positive electrodes of two adjacent PAs. However, the interplay among Re_θ, $\overline{W}_{max}^+$ and L^+ was not studied.

This work presents an experimental investigation on DR following Cheng *et al.* (2021*b*) and the analysis of available data produced from PGSVs in the literature, focusing on the inter-relationships between $\overline{W}_{max}^+$, L^+ and Re_τ. Theoretical analysis is conducted on the relationship between DR and the strength of PGSVs, which leads to the finding of the empirical scaling law of the TBL control based on the PA. The paper is organized as follows. Experimental details are provided in §2. The DR results and particle image velocimetry (PIV) measurements are presented in §3, with a focus on the dependence of DR on individual control parameters. Section 4 presents a scaling law for the DR, along with theoretical analysis, and inferences from this law. The results are summarized and concluded in §5.

2. Experimental details

2.1. *Generation of fully developed TBLs*

The experimental set-up to generate fully developed TBLs (figure 1*a*) is the same as described in Cheng *et al.* (2021*b*). The characteristic parameters of the TBL at the free-stream velocity $U_\infty = 2.4$–5.0 m s^{-1} are given in table 1, including the TBL disturbance thickness δ, friction velocity u_τ, viscous length scale δ_υ ($= \upsilon / u_\tau$, where υ is the kinematic viscosity) and Re_τ based on u_τ. Unless otherwise stated, the superscript '+' in this paper denotes normalization by the inner scales in the absence of control. The coordinate system (x, y, z) is defined in figure 1, with the origin at the mid-point of the trailing edge of the PA array. The instantaneous velocities along the x, y and z directions are denoted by U, V and W, respectively.

2.2. *Plasma-actuator array*

The PA array (figure 1*b*) to generate counter-rotating streamwise vortices is similar to configuration B in Cheng *et al.* (2021*b*). However, the dielectric panel is made up of one layer of 0.2 mm thick mica paper to replace Mylar and Kapton tapes used in Cheng *et al.* (2021*b*). As a result, it is possible to use the FE force balance to capture the real-time friction drag variation in the actuation area. The PA is placed on the FE (210 mm × 240 mm) of our newly improved force balance where the load cell is well isolated from the thermal and electrical effects associated with the PA. The plasma actuation is generated by using a sinusoidal-AC waveform applied with a voltage $E_{p-p} = 1.2$–6.0 kV$_{p-p}$ (subscript '*p–p*' denotes peak-to-peak). Following Cheng *et al.* (2021*b*), the frequency of E_{p-p} is fixed at 11 kHz, which is the optimum operating frequency of
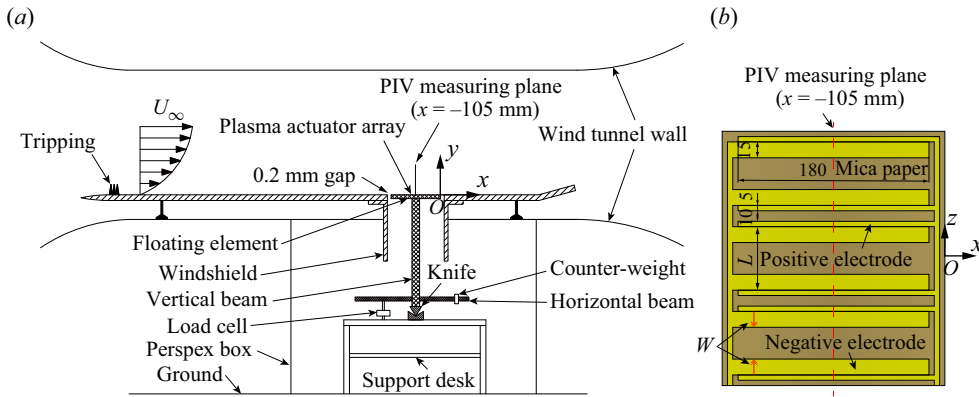
Figure 1. (*a*) Schematic of experimental set-up for the generation of a TBL and the floating-element (FE) balance. (*b*) Top view of schematic of the PA array (not to scale; dimensions are in millimetres).

U_∞ (m s^{-1})	δ (mm)	Re_τ	u_τ (m s^{-1})	δ_υ (mm)
2.4	80	564	0.111	0.142
3.0	70	612	0.137	0.114
3.6	65	658	0.154	0.102
4.3	63	741	0.185	0.085
5.0	63	811	0.202	0.078

Table 1. Characteristic parameters of the uncontrolled TBL.

the power supply. As illustrated in figure 1(*b*), the total streamwise length of the PA array is 210 mm, and its effective length (excluding a length of 15 mm at each end for wire connection) is 180 mm. The distance L between the positive electrodes of two adjacent PAs or one pair of PAs is 60 mm which has been demonstrated to be optimal in Cheng *et al.* (2021*b*). The plasma-generated forcing is unsteady, with the same frequency as the power supply signal, and produces a series of compressional waves, originating at the junction of the positive and negative electrodes. The wave exhibits only spanwise dependence, resulting in a spanwise wall jet (Thomas *et al.* 2019).

2.3. *High-resolution FE force balance*

The high-resolution FE force balance developed by Cheng *et al.* (2021*b*) is significantly improved in the present work (figure 1). The FE material has been changed from a 1 mm thick carbon fibre plate to a 2 mm thick anti-static Bakelite plate with an electric resistance range of 10^8-10^{10} Ω. This anti-static Bakelite plate is connected to the ground without tension through a copper foil with a width of 5 mm and a thickness of 0.05 mm, which can shield the plasma-generated electromagnetic and thermal interference and secure reliable load cell measurements. The force balance employs an adjustment system introduced in Wei *et al.* (2024), which allows for a very small clearance (0.2 mm) between the FE and the flat plate. Such a small clearance effectively minimizes errors associated with the pressure forces on the lip and surface of the FE. The force balance is calibrated using the skin-friction drag on the FE measured over a range of U_∞, as proposed by Cheng *et al.* (2021*b*). The mean drag variation generated by PGSVs under identical experimental conditions is determined from 12 repeated measurements, each over a duration of 30 s that follows a

60 second operation of the PA array to ensure data is taken during the steady state of PA discharge.

2.4. *PIV measurements*

A Dantec PIV system is used to measure flow in the y–z plane of $x = -105$ mm at $U_\infty = 2.4$ m, 3.6 m and 5.0 m s^{-1}. The flow is illuminated using a 3.0 mm thick laser sheet shining through the wind tunnel view window (optical glass), produced by a dual beam laser source (Beamtech Vlite-200, with a maximum frequency and pulse energy of 15 Hz and 200 mJ, respectively) in conjunction with spherical and cylindrical lenses. A high-quality mirror of 80 mm $\times$ 150 mm is fixed on the plate at $x = 0.51$ m, 45° with respect to the y–z plane, downstream of the PA so that the images in the plane can be captured using a camera (Imager pro HS4M, 4 megapixel sensors, 2016 $\times$ 2016 pixels resolution) placed outside the working section. The image covers an area of 80 mm $\times$ 80 mm. The total number of images captured is 2000 pairs with a sampling frequency of 15 Hz.

3. Experimental results

3.1. *Dependence of DR on flow and control parameters*

The spatially averaged DR on the FE is measured using the force balance (figure 1a). The DR is evaluated through $\Delta F = (F_{on} - F_{off})/F_{off}$, where F is the skin-friction drag on the FE, and subscripts 'on' and 'off' denote the cases with and without control, respectively. The ΔF depends on E_{p-p} imposed as well as on Re_τ as shown in figure 2(a), where the dashed line is a least-square fitting curve (cubic polynomial) to the data. In general, ΔF dips with increasing E_{p-p} for $Re_\tau = 564$–811. With increasing E_{p-p}, the PGSVs and associated spanwise wall jets are strengthened, resulting in a more pronounced DR (Yao *et al.* 2018). The maximum DR of all Reynolds numbers occurs at $E_{p-p} = 5.6$–6.0 kV$_{p-p}$. However, ΔF increases or DR diminishes with increasing Re_τ, from 70 % at $Re_\tau = 564$ to only 18 % at $Re_\tau = 811$. This drop is attributed to the weakened strength of PGSVs at higher Re_τ compared with their lower Re_τ counterparts, which will be discussed in detail in §3.2. Evidently, ΔF exhibits a logarithmic decrease with a rise in the maximum spanwise mean velocity $\overline{W}_{max}^+$ for a given Re_τ, as shown in figure 2(b), where W is measured in the absence of flow. This finding stands in stark contrast to that of Thomas *et al.* (2019), who reported a linear relationship between ΔF and $\overline{W}_{max}^+$ for the PGSVs over the range of $Re_\theta = 4538$–$11\,636$. Their result is probably attributed to their imposed 'spikes' by plasma forcing and narrow range of $\overline{W}_{max}^+$, from 0.4 to 1.6, much smaller than the present range of 0.01–6.87.

The ΔF depends further on L^+ and Re_τ (figure 2c,d). The data for this study and Thomas *et al.* (2019) are least-squares-fitted to a cubic polynomial. Their PA array generated co-rotating streamwise vortices, different from the present counter-rotating streamwise vortices. Evidently, DR decreases with the increasing L^+ or Re_τ for a given $\overline{W}_{max}$, be it the present data or Thomas *et al.*'s (2019) data. Noting $Re_\tau = u_\tau \delta/\upsilon = \delta/\delta_\upsilon = \delta^+$, Re_τ is in the wall unit as L^+. In fact, the dependence of ΔF on Re_τ is quite similar to that on L^+.

3.2. *Plasma-induced flow structure*

Each PA generates one pair of counter-rotating streamwise vortices, as is evident in the PIV images (figure 3) captured half-way through the PA array, i.e. $x = -105$ mm (figure 1b). At $Re_\tau = 564$ or $x^+ = -741$, the maximum vorticity $|\overline{\omega_x^+}|_{max}$ is approximately
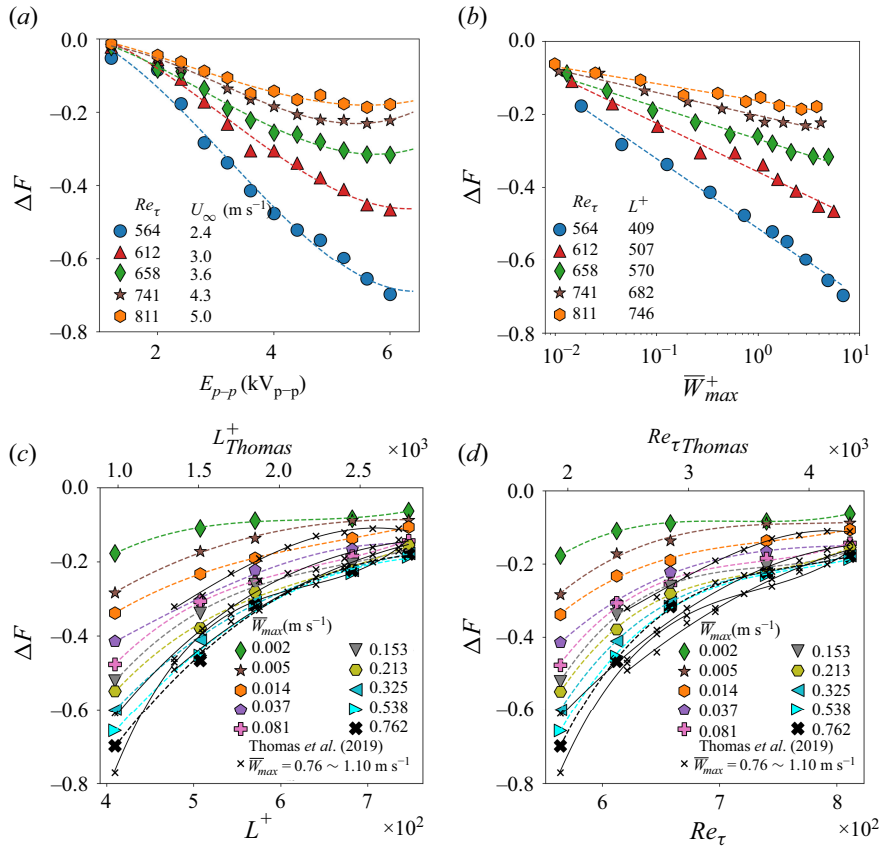
Figure 2. Dependence of drag variation ΔF on (a) E_{p-p}, (b) $\overline{W}_{max}^{+}$, (c) L^{+} and (d) Re_τ. L_{Thomas}^{+} and $Re_{\tau Thomas}$ are the values of L^{+} and Re_τ in Thomas *et al.*'s (2019) experiments. The broken and solid curves are cubic polynomial fits to the present and Thomas *et al.* (2019) data, respectively.

0.42. However, at $Re_\tau = 685$ or $x = -1032$ and $Re_\tau = 811$ or $x^{+} = -1352$, $\overline{|\omega_x^{+}|}_{max}$ drops to only 0.24 and 0.18, respectively. The PGSVs at $Re_\tau = 564$ appear strong, as manifested by their size and vorticity concentration, thus inducing oppositely signed vorticity concentrations around them. This phenomenon is not evident at the higher Re_τ when the PGSVs weaken in strength (figure 3b,c). This weakened strength at higher Re_τ is internally consistent with a decrease in DR with increasing Re_τ (figure 2a,b). Note that the cross-sectional area $L^{+} \times Re_\tau = L^{+} \times \delta^{+}$ of the TBL gradually grows with increasing Re_τ, implying that the area under the influence of PGSVs contracts at a higher L^{+} or Re_τ, with respect to the cross-sectional area of the TBL, which also accounts for the diminished effect of PGSVs and the decreased DR for higher L^{+} or Re_τ (figure 2c,d).

4. Theoretical consideration

Vorticity concentrations, as seen in figure 3, originate from the surface of the flat plate, moving with respect to fluid, under the viscosity effect and the no-slip condition (Wu & Wu 1996). In this section, we attempt to understand the generation of skin-friction drag and its reduction based on vorticity dynamics on the boundary between the solid surface and fluid.

(a)

(b)

(c)
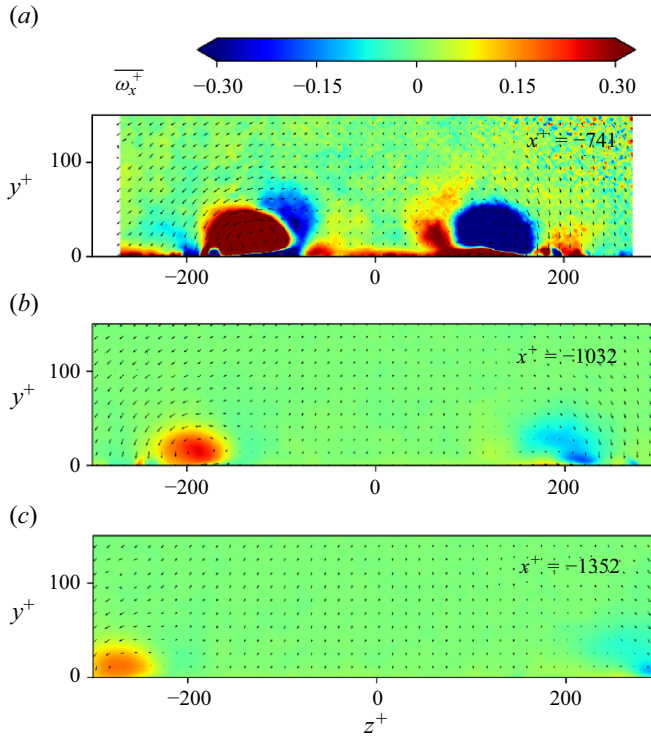
Figure 3. Time-averaged velocity vectors $(\overline{V^+}, \overline{W^+})$ and isocontours of vorticity $\overline{\omega_x^+}$ $\overline{\omega_x^+} = \overline{\mathrm{d}V^+/\mathrm{d}z^+} - \overline{\mathrm{d}W^+/\mathrm{d}y^+}$ $\overline{\mathrm{d}W^+/\mathrm{d}y^+}$ in the y–z plane at the centre ($x = -105$ mm) of the PA array. Here (a) $Re_\tau = 564$, (b) 658 and (c) 811. The applied voltage on PAs is 6.0 kV$_{\mathrm{p\text{-}p}}$.

On a surface S with unit normal vector $\boldsymbol{n}$, either inside the fluid or on the boundary, the surface stress may be given following a triple decomposition by

$$\boldsymbol{t} \equiv \boldsymbol{n} \cdot \boldsymbol{T} = -\Pi\boldsymbol{n} + \boldsymbol{\tau} + \boldsymbol{t}_s, \qquad (4.1)$$

where $\boldsymbol{T}$ is the stress tensor. The terms on the right-hand side of (4.1) are the normal stress, shear stress and surface-deformation stress, respectively, from left to right, and may be written as

$$-\Pi\boldsymbol{n} = -[p - (\lambda + 2\mu)\boldsymbol{\nabla} \cdot \boldsymbol{u}]\boldsymbol{n}, \qquad (4.2a)$$
$$\boldsymbol{\tau} = \mu\boldsymbol{\omega} \times \boldsymbol{n}, \qquad (4.2b)$$
$$\boldsymbol{t}_s = -2\mu\boldsymbol{n} \cdot [(\boldsymbol{\nabla} \cdot \boldsymbol{u})\boldsymbol{I} - \boldsymbol{\nabla}\boldsymbol{u}^T], \qquad (4.2c)$$

where p is the pressure, λ is the second dynamic viscosity that can be dropped out from the equation for an incompressible fluid, μ is dynamic viscosity, $\boldsymbol{u}$ is the flow velocity vector, $\boldsymbol{u}^T$ is the transpose of $\boldsymbol{u}$, $\boldsymbol{\nabla}$ is the differential operator, $\boldsymbol{\omega} = \boldsymbol{\nabla} \times \boldsymbol{u}$ is the vorticity vector and $\boldsymbol{I}$ is the unit tensor. Following the Stokes–Helmholtz decomposition, the divergence of $\boldsymbol{T}$ in (4.1) is given by

$$\boldsymbol{\nabla} \cdot \boldsymbol{T} = -\boldsymbol{\nabla}\Pi - \mu(\boldsymbol{\nabla} \times \boldsymbol{\omega}), \qquad (4.3)$$

where the first and second terms on the right-hand side represent the compression and shear variation, respectively. Taking the curl of (4.3) and applying the continuity equation, we may obtain the following vorticity equation:

$$\rho \frac{\mathrm{D}}{\mathrm{D}t}\left(\frac{\boldsymbol{\omega}}{\rho}\right) = \boldsymbol{\omega} \cdot \nabla \boldsymbol{u} + \nabla \times \boldsymbol{f} + \frac{1}{\rho^2}\nabla\rho \times \nabla\Pi - \frac{\mu}{\rho}\nabla \times (\nabla \times \boldsymbol{\omega}), \qquad (4.4)$$

where ρ is the density of fluid. Thus, the total vorticity variation in a control volume V bounded by S is given by

$$\int_V \frac{\mathrm{D}\boldsymbol{\omega}}{\mathrm{D}t}\mathrm{d}V = \frac{\mathrm{d}}{\mathrm{d}t}\int_V \boldsymbol{\omega}\mathrm{d}V$$
$$= \int_V \left(\boldsymbol{\omega} \cdot \nabla \boldsymbol{u} + \frac{1}{\rho^2}\nabla\rho \times \nabla\Pi\right)\mathrm{d}V + \oint_S \boldsymbol{n} \times \boldsymbol{f}\mathrm{d}S - \oint_S \upsilon\boldsymbol{n} \times (\nabla \times \boldsymbol{\omega})\mathrm{d}S. \qquad (4.5)$$

The volume integral on the right-hand side of (4.5) includes contributions from vorticity stretching and turning and the baroclinicity, and the first surface integral is due to a non-conservative force $\boldsymbol{f}$. The integrand of the second surface integral is the boundary vorticity flux (BVF) (Lyman 1990). Using the vector identity, the volume integral of $\boldsymbol{\omega}$ can be expressed in terms of the tangential velocity along the boundary, yielding

$$\boldsymbol{\varGamma} = \int_V \boldsymbol{\omega}\mathrm{d}V = \int_V \nabla \times \boldsymbol{u}\mathrm{d}V = \oint_S \boldsymbol{n} \times \boldsymbol{u}\mathrm{d}S, \qquad (4.6)$$

where $\boldsymbol{\varGamma}$ is the vector circulation (Terrington *et al.* 2022; Wu & Wu 1996). Then, on substitution of (4.6) into (4.5), we obtain the following equation:

$$\frac{\mathrm{d}\boldsymbol{\varGamma}}{\mathrm{d}t} = \int_V \left(\boldsymbol{\omega} \cdot \nabla \boldsymbol{u} + \frac{1}{\rho^2}\nabla\rho \times \nabla\Pi\right)\mathrm{d}V + \oint_S \boldsymbol{n} \times \boldsymbol{f}\mathrm{d}S - \oint_S \upsilon\boldsymbol{n} \times (\nabla \times \boldsymbol{\omega})\mathrm{d}S. \quad (4.7)$$

The BVF in (4.7) represents a transfer of circulation due to the tangential viscous acceleration of fluid on the boundary between two adjacent volumes. Based on Newton's Second Law, the flow tangential acceleration is directly connected to the force associated with the wall shear stress. Since the wall shear stress in (4.2*b*) originates from the generation of vorticity, the BVF can be regarded as the origin of skin friction in a TBL (Wang *et al.* 2022). As such, of particular interest is the change of the viscous term in (4.7), which should be linked directly to a variation in skin friction, say, under control, viz.

$$\boldsymbol{\Delta F} = \boldsymbol{F_{on}} - \boldsymbol{F_{off}} = g(\boldsymbol{\varGamma'}), \qquad (4.8)$$

where $\boldsymbol{\varGamma'} = [\oint_S \upsilon\boldsymbol{n} \times (\nabla \times \boldsymbol{\omega})\mathrm{d}S]_{on} - [\oint_S \upsilon\boldsymbol{n} \times (\nabla \times \boldsymbol{\omega})\mathrm{d}S]_{off}$.

Under the present plasma control, the vorticity vector $\boldsymbol{\omega} = [\omega_x, \omega_y, \omega_z]$ is predominantly along the streamwise direction due to the generation of PGSVs, and ω_y and ω_z are both negligibly small, compared with ω_x, within the control volume dominated by PGSVs. That is, the vorticity vector can be written as $\boldsymbol{\omega} \approx [\omega_x, 0, 0]$. Assuming vorticity is conserved, the change in the BVF over the closed control surface which should be adequately large to enclose all the boundary vorticity flux generated by the PA, as given in (4.8), may be estimated approximately by the integral of ω_x in the y–z plane largely associated with the PGSV, viz.

$$\varGamma' \approx \oint_{S_p} \omega_x\mathrm{d}y\mathrm{d}z, \qquad (4.9)$$

where S_p is the surface in the y–z plane where the PGSVs may be adequately captured. The term on the right-hand side of (4.9) is the circulation or strength of PGSVs and can be determined from the PIV data measured in the y–z plane. In view of the limited PIV-measurement resolution, we introduce a threshold r that determines the border of the

PGSVs, i.e. $|\overline{\omega_x^+}| > r|\overline{\omega_x^+}|_{max}$ within the PGSV. Then the wall-unit normalized circulation of the PGSVs can be written as

$$\Gamma_r'^+ \approx \oint_{S_r} \omega_x^+ \mathrm{d}y^+ \mathrm{d}z^+, \tag{4.10}$$

where S_r is the size of the PGSV.

5. Scaling of DR

Theoretical analysis leads to a finding that the DR depends on only one physical quantity, namely, the variation in the summation of vorticity or circulation within the control volume (4.8). Under control, this variation in circulation is ascribed to the presence of PGSVs (4.9), i.e. due to the artificially generated circulation (4.9) associated with PGSVs. This finding points to the fact that $\Delta F = g_1(\overline{W}_{max}^+, L^+, Re_\tau)$, as observed from figure 2, may be reduced to $\Delta F = g_2(\xi)$. However, g_1 is an unknown function; it is also a challenge to determine the function g_2 and the scaling factor ξ. Fortunately, we have a great amount of experimental data from a physical system. After careful analysis of the experimental data and numerous trial-and-error attempts, we eventually find that $\Delta F = -3.8 \times 10^4 \xi$ (figure 4), where

$$\xi = \frac{k_2 \log_{10}\left(k_1 \overline{W}_{max}^+\right)}{L^+ Re_\tau} = \frac{k_2 \log_{10}\left(k_1 \overline{W}_{max}^+\right)}{L^+ \delta^+}. \tag{5.1}$$

Note that the flow field of the predominantly two-dimensional vortex may be decomposed into the radial and tangential motions, and the vortex strength (or circulation) and the maximum tangential velocity are statistically linked to each other (e.g. Zhou & Antonia 1993). Furthermore, the spanwise motion and $\overline{W}_{max}^+$ originate largely from PGSVs. Then, it seems plausible that the numerator of (5.1) is connected to the circulation of PGSVs, and ξ may be interpreted as the circulation per unit area or strength of PGSVs. Interestingly, Thomas *et al.*'s (2019) data also collapse quite well about this line provided $k_1 = 10^3$ and $k_2 \approx 15$. Furthermore, we may estimate $\Gamma_r'^+$ ($r = 0.1$) from the PIV data measured at three Reynolds numbers discussed in §3.2. In the calculation of $\Gamma_r'^+$, we use the absolute values of ω_x^+ to avoid the cancellation of oppositely signed vorticity values associated with the counter-rotating PGSVs. Surprisingly, the dependence of ΔF on $\Gamma_r'^+$ also collapses well about this line once the value of $\Gamma_r'^+$ is scaled down by a factor of 2.5×10^{-8}, i.e. $2.5 \times 10^{-8} \Gamma_r'^+$. That is, $\Delta F = g_1(\overline{W}_{max}^+, L^+, Re_\tau)$ can be also reduced to $\Delta F = g_2(2.5 \times 10^{-8} \Gamma_r'^+)$. All the results demonstrate the reliability and robustness of the scaling law (5.1). The empirical data analysis again demonstrates unequivocally that the DR is proportional to the strength of PGSVs. Clearly, ΔF drops or DR increases almost linearly with growing ξ. Note that the Re_τ effect is embedded in $\overline{W}_{max}^+$ and L^+ because the two parameters are both normalized by wall units that are directly related to Re_τ.

Some remarks are due on the scaling law. In the present study, a sine-AC actuation signal was used, while Thomas *et al.* (2019) deployed pulsed-DC actuation. The latter can generate a much higher instantaneous plasma-induced spanwise wall-jet velocity, compared with the sine-AC actuation, and hence a higher value of k_2. Furthermore, the present PAs generate counter-rotating streamwise vortices, whereas Thomas *et al.* (2019) produced co-rotating streamwise vortices. This difference may also account for the different k_2 values in (5.1) or figure 4 between the two studies. It is worth commenting on the departure of experimental data from $\Delta F = -3.8 \times 10^4 \xi$ at large ξ (figure 4). Two
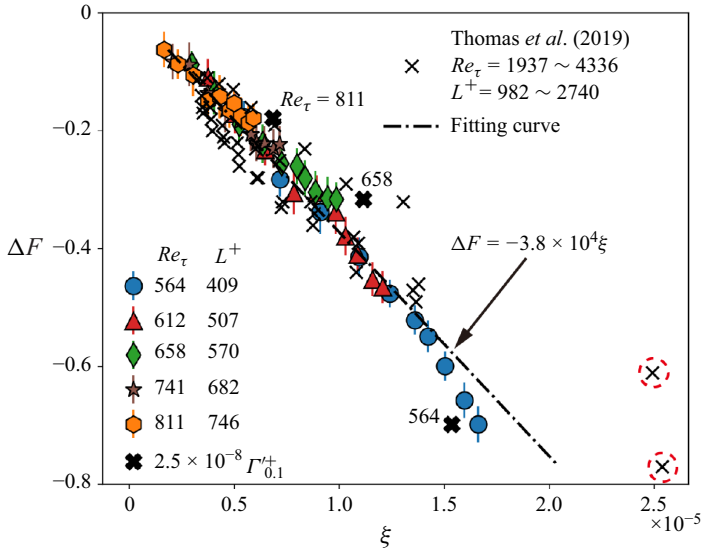
Figure 4. Dependence of drag variation ΔF on $\xi = [k_2 \log_{10}(k_1 \overline{W}_{\max}^+)]/(L^+ Re_\tau)$, where $k_1 = 10^3$ and $k_2 \approx$ 1 for the present results and $k_1 = 10^3$ and $k_2 \approx 15$ for the Thomas *et al.*'s (2019) results. The black cross symbols are 2.5×10^{-8} times the measured circulation $\Gamma'^+_{0.1}$ of the PGSV, whose border is defined at $\overline{|\omega_x^+|} = 0.1\overline{|\omega_x^+|}_{max}$ ($E_{p-p} = 6$ kV$_{p-p}$ and $Re_\tau = 564$, 658 and 811). The large departure of two data points from Thomas *et al.* (2019) are marked by dashed circles. The error bars denote the standard deviation out of 12 repeated measurements.

factors may contribute to this departure. Firstly, the vortex strength grows with increasing E_{p-p}. So does ξ. Beyond a certain level of E_{p-p}, the vortices grow in strength rapidly, causing a rise in vortex-induced drag in the TBL (Schoppa & Hussain 1998; Iuso *et al.* 2002). Secondly, the large vortex strength at large ξ implies enhanced interactions between neighbouring PGSVs and hence the cancellation effect becomes more appreciable. Both factors cause experimental data below the fitting curve. It is worth commenting on the large departure of two data points (marked by dashed circles), extracted from Thomas *et al.* (2019), from the scaling law in figure 4. These points were obtained at relatively low Re_τ and showed appreciable deviation from their other data (their figure 15). This deviation arises from a limited resolution, approximately 0.04 g, in their force balance, which is inadequate to capture a very small skin-friction drag of 0.029 g at $Re_\tau = 1937$ (Thomas *et al.* 2019).

Several interesting inferences can be made from the scaling law. Firstly, given two of the three parameters $\overline{W}_{max}^+$, L^+ and Re_τ, the dependence of ΔF on the remaining parameter may be determined from the scaling law. For example, given L^+ and Re_τ, ΔF drops or DR rises logarithmically with increasing $\overline{W}_{max}^+$, as measurements (figure 2a) indicate. Evidently, the relationship between ΔF and L^+ or Re_τ derived from the scaling law is also as in figure 2(b,c). With ΔF and $\overline{W}_{max}^+$ given, we may also determine the relation between L^+ and Re_τ. Thus, the scaling law provides a powerful tool for the PA design and also the control performance prediction. Secondly, given ξ or ΔF, $\overline{W}_{max}^+$ diminishes with decreasing L^+ or Re_τ, implying less energy consumption and thus higher control efficiency. Figure 5(a) presents the dependence of ΔF on $\overline{W}_{max}^+$ and $L^+ Re_\tau$. The control efficiency $\eta = (F_{on} - F_{off})U_\infty/P_{input}$ is also given in the figure, as marked by the thick
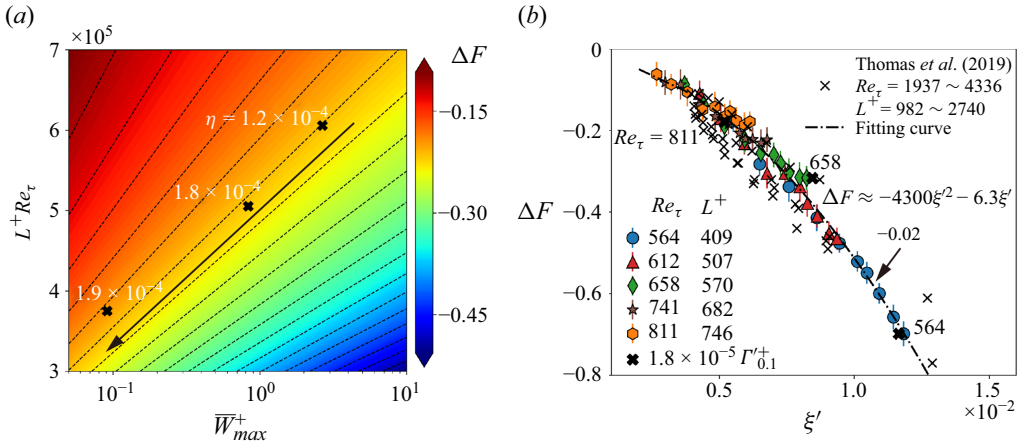
Figure 5. (a) Dependence of ΔF on $\overline{W}^+_{max}$ and $L^+ Re_\tau$. The control efficiency η estimated at $\Delta F \approx -0.185$ is given at three points, marked by black crosses. The dotted lines are the isocontours of ΔF and the arrow indicates the direction of increasing η. (b) Dependence of drag variation ΔF on ΔF. The black crosses mark the measured circulation $\Gamma'^+_{0.1} \times 1.8 \times 10^{-5}$ of the PGSV, whose border is defined at $|\overline{\omega_x^+}| = 0.1|\overline{\omega_x^+}|_{max}$. The error bars denote the standard deviation out of 12 repeated measurements.

black crosses, where P_{input} is the power consumption determined by the Q–V cycloramas (Lissajous figure) measured through two parallel- and series-connected capacitances at $\Delta F \approx -0.185$. Evidently, η drops with the shrinking $L^+ Re_\tau$ and $\overline{W}^+_{max}$. Thirdly, Thomas *et al.* (2019) proposed $\Delta F = g_3(L^+, \overline{W}^+_{max})$, where g_3 was a unknown function and the effect of Re_τ on ΔF was not considered. Indeed, the ΔF–L^+ and ΔF–Re_τ relationships are similar, as shown in figure 2(c,d). In fact, L^+ and Re_τ are strictly nonlinear. However, this nonlinearity is very weak. Readers are cautioned that further experiments need to be conducted should this approximate linearity be extended beyond the range of $Re_\tau = 564 \sim 4336$ presently examined. Consequently, ξ can be further simplified to $\xi' = [k_2 \log_{10}(k_1 \overline{W}^+_{max})]/L^+$ (figure 5b), where $k_1 = 10^4$ and $k_2 \approx 1$ for the present data and $k_1 = 10^4$ and $k_2 \approx 3$ for Thomas *et al.*'s (2019) data. This simplified equation involves only two parameters, thus facilitating calculation and analysis in predicting DR. The least-squares fitting curve is now given by $\Delta F = g_3(\xi') \approx -4300\xi'^2 - 6.3\xi' - 0.02$. Note that $2.5 \times 10^{-8} \Gamma'^+_{0.1}$ in figure 4 is now $1.8 \times 10^{-5} \Gamma'^+_{0.1}$ in figure 5(b). Finally, DR can be predicted once ξ or ξ' is known or vice versa. By determining the value of ξ or ΔF, the magnitudes of the applied voltages can be adjusted precisely in accordance with Re_τ to achieve the optimal plasma-induced velocity, thereby attaining the desired specific DR. This approach also aids in the design of PA arrays, such as the choice of L^+.

6. Conclusions

The TBL control is conducted experimentally at $Re_\tau = 564$–811 using a spanwise array of longitudinal dielectric barrier discharge PAs, with a view to reducing skin friction and finding the scaling law for DR. The following conclusions can be drawn out of this work.

(i) The dependence of DR on three control parameters is investigated, including Re_τ, E_{p-p} or $\overline{W}^+_{max}$ and L^+. For a given Re_τ, DR grows logarithmically with higher $\overline{W}^+_{max}$, which corresponds to the strength of PGSVs. This finding differs from the previously reported linear relationship (Thomas *et al.* 2019). The discrepancy is ascribed to the

available data range of $\overline{W}_{max}^{+}$, which is large presently but small previously. On the other hand, for the given $\overline{W}_{max}$, DR decreases with increasing L^{+} or Re_{τ} due to a contraction in the normalized area under the influence of PGSVs. A similar observation was made by Thomas *et al.* (2019) in spite of their different configuration of PAs that generate co-rotating streamwise vortices.

(ii) It has been found for the first time from theoretical and empirical scaling analyses of obtained experimental data that the dimensionless drag variation $\Delta F = g_1(\overline{W}_{max}^{+}, L^{+}, Re_{\tau})$ can be reduced to $\Delta F = g_2(\xi) = -3.8 \times 10^4 \xi$, where the scaling factor $\xi = [k_2 \log_{10}(k_1 \overline{W}_{max}^{+})]/(L^{+} Re_{\tau})$ and $k_1 = 10^3$ and $k_2 \approx 1$ based on the present data or $k_1 = 10^3$ and $k_2 \approx 15$ based on Thomas *et al.*'s (2019) data. This factor is physically the circulation or strength of PGSVs, as confirmed theoretically. As a matter of fact, it is found from experimental data that $\Delta F = g_2(2.5 \times 10^{-8} \Gamma_{0.1}'^{+})$, where $\Gamma_{0.1}'^{+}$ is the circulation based on the PGSVs, whose border is defined at $|\omega_x^{+}| = 0.1|\omega_x^{+}|_{max}$. The difference in k_2 between the present and Thomas *et al.*'s (2019) studies is attributed to different power supplies and PA configurations used in the two investigations.

(iii) Several inferences are made from the scaling law. Firstly, given two of $\overline{W}_{max}^{+}$, L^{+} and Re_{τ}, the effect of the third parameter on ΔF may be determined from the scaling law. Secondly, given ξ or ΔF, the control efficiency rises with a decrease in the product of L^{+} and Re_{τ} or the area $L^{+}\delta^{+}$, which implies a smaller $\overline{W}_{max}^{+}$ required and hence less energy consumption. Thirdly, noting the similarity between the ΔF–L^{+} and ΔF–Re_{τ} relationships (figure 2*c,d*), ξ can be simplified to $\xi' = [k_2 \log_{10}(k_1 \overline{W}_{max}^{+})]/L^{+}$ by removing Re_{τ}. Finally, DR may be predicted given ξ or ξ' or vice versa, thus providing a theoretical guideline for the design of PA arrays when the DR and Reynolds numbers are specified.

Declaration of interests. The authors report no conflict of interest.

REFERENCES

CHENG, X.Q., QIAO, Z.X., ZHANG, X., QUADRIO, M. & ZHOU, Y. 2021*a* Skin-friction reduction using periodic blowing through streamwise slits. *J. Fluid Mech.* **920**, A50.

CHENG, X.Q., WONG, C.W., HUSSAIN, F., SCHRÖDER, W. & ZHOU, Y. 2021*b* Flat plate drag reduction using plasma-generated streamwise vortices. *J. Fluid Mech.* **918**, A24.

CHOI, H., MOIN, P. & KIM, J. 1993 Direct numerical simulation of turbulent flow over riblets. *J. Fluid Mech.* **255**, 503–539.

FUKAGATA, K., KERN, S., CHATELAIN, P., KOUMOUTSAKOS, P. & KASAGI, N. 2008 Evolutionary optimization of an anisotropic compliant surface for turbulent friction drag reduction. *J. Turbul.* **9**, 1–7.

IUSO, G., ONORATO, M., SPAZZINI, P.G. & CICCA, G.M.D. 2002 Wall turbulence manipulation by large-scale streamwise vortices. *J. Fluid Mech.* **473**, 23–58.

KLINE, S.J., REYNOLDS, W.C., SCHRAUB, F.A. & RUNSTADLER, P.W. 1967 The structure of turbulent boundary layers. *J. Fluid Mech.* **30** (4), 741–773.

LYMAN, F.A. 1990 Vorticity production at a solid boundary. *Appl. Mech. Rev.* **43**, 157–158.

QUADRIO, M., RICCO, P. & VIOTTI, C. 2009 Streamwise-travelling waves of spanwise wall velocity for turbulent drag reduction. *J. Fluid Mech.* **627**, 161–178.

RASTEGARI, A. & AKHAVAN, R. 2015 On the mechanism of turbulent drag reduction with super-hydrophobic surfaces. *J. Fluid Mech.* **773**, R4.

SCHOPPA, W. & HUSSAIN, F. 1998 A large-scale control strategy for drag reduction in turbulent boundary layers. *Phys. Fluids* **10** (5), 1049–1051.

TERRINGTON, S.J., HOURIGAN, K. & THOMPSON, M.C. 2022 Vorticity generation and conservation on generalised interfaces in three-dimensional flows. *J. Fluid Mech.* **936**, A44.

THOMAS, F.O., CORKE, T.C., DUONG, A.H., MIDYA, S. & YATES, K. 2019 Turbulent drag reduction using pulsed-DC plasma actuation. *J. Phys. D: Appl. Phys.* **52** (43), 434001.

WANG, M., EYINK, G.L. & ZAKI, T.A. 2022 Origin of enhanced skin friction at the onset of boundary-layer transition. *J. Fluid Mech.* **941**, A32.

WEI, X.H., ZHANG, X., CHEN, J.G. & ZHOU, Y. 2024 An air-bearing floating-element force balance for friction drag measurement. *J. Fluids Engng* **146** (6), 061501.

WEI, X.H. & ZHOU, Y. 2024 Scaling of skin-friction reduction based on plasma-generated streamwise vortices. In *Fluid-Structure-Sound Interactions and Control, Proceedings of the 6th Symposium on Fluid-Structure-Sound Interactions and Control (FSSIC 2023)*, (eds. D. Kim, K.C. Kim, Y. Zhou & L. Huang) pp. 25–30. Springer Nature Singapore.

WU, J.Z. & WU, J.M. 1996 Vorticity dynamics on boundaries. In *Advances in Applied Mechanics*, vol. 32, pp. 119–275. Elsevier.

YAO, J., CHEN, X. & HUSSAIN, F. 2018 Drag control in wall-bounded turbulent flows via spanwise opposed wall-jet forcing. *J. Fluid Mech.* **852**, 678–709.

ZHOU, Y. & ANTONIA, R.A. 1993 A study of turbulent vortices in the near wake of a cylinder. *J. Fluid Mech.* **253**, 643–661.